

# Multiresolution Time-Domain Analysis of Plane-Wave Scattering From General Three-Dimensional Surface and Subsurface Dielectric Targets

Xianyang Zhu, *Member, IEEE*, and Lawrence Carin, *Fellow, IEEE*

**Abstract**—The multiresolution time domain (MRTD) is used to analyze wide-band plane-wave scattering from general dielectric targets embedded in a lossy half-space, with free-space scattering as a special case. A Haar wavelet expansion is used for simplicity, this constituting a generalization of the widely used finite-difference time-domain (FDTD) method. In addition to developing the mathematical formulation, example results are presented for several targets, with the MRTD results validated through comparison with an independent frequency-domain method-of-moments solution and an FDTD model.

**Index Terms**—Buried object detection, electromagnetic scattering, multiresolution techniques, time-domain analysis.

## I. INTRODUCTION

SUBSURFACE sensing is of interest for many applications, including detection of buried pipes, unexploded ordnance (UXO), and land mines [1]–[7]. There has consequently been significant interest in the development of modeling tools for the analysis of electromagnetic-based subsurface sensing, with application to radar [1]–[4] and electromagnetic induction [5]. In particular, authors have considered both frequency- and time-domain models, the former including the method of moments (MoM) [3], [4], the extended-Born method [5], and fast-multipole methods [6]. With regard to time-domain methods, the finite-difference time-domain (FDTD) method has been applied widely [2], [7]. The aforementioned frequency-domain methods typically employ a Green's function (e.g., for layered media or a half-space [3]–[6]), and therefore they assume some regularity in the background medium. The advantage of such an approach is that one need only discretize the target surface, rather than the entire region of interest, yielding computational efficiency. By contrast, the FDTD discretizes the entire computational domain, in both space and time, and therefore it is applicable to very general background media [2], [7].

The FDTD can be viewed in terms of a pulse expansion of the electromagnetic fields, in both space and time [8]. With this understanding, one can generalize the FDTD by considering an alternative expansion. For example, there has recently been in-

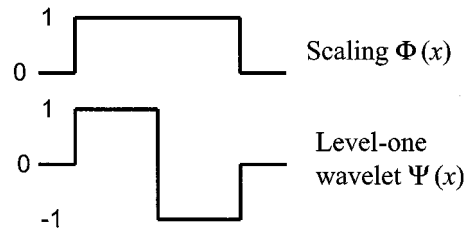


Fig. 1. Haar scaling function and first-level wavelet on one dimension.

terest in expanding the fields in terms of a wavelet basis, thus realizing what has been termed a multiresolution time-domain (MRTD) analysis [8], [9]. The multiresolution property is a consequence of the wavelet expansion, with the lowest resolution manifested in terms of scaling functions, with higher resolution (refinement) added by wavelets. Wavelets of successively higher resolution can be added to the scaling-function expansion to realize a field representation of a desired resolution. There are an infinite number of possible orthogonal or biorthogonal wavelet classes [10], but one typically imposes requirements (e.g., differentiability and/or vanishing low-order moments [10]) that restrict the wavelet form. As illustrated further in Section II, one of the important requirements of the scaling and wavelet functions, in the context of MRTD, is that they have compact support (zero outside a prescribed region).

With regard to the choice of scaling and wavelet functions, for implementation of the MRTD, one can consider smooth functions such as the Battle–Lemarie [8], [9] orthogonal wavelets or the Cohen–Daubechies–Fouveau [10], [11] biorthogonal wavelets. The Battle–Lemarie wavelets are not of strictly compact support, although these infinite-support functions can be truncated approximately in the context of MRTD [8], [9]. In this paper, we focus on the simpler Haar wavelets, the scaling function and mother wavelet for which are shown in Fig. 1 (in one dimension). One notices that the Haar scaling function is simply the pulse expansion used in the traditional FDTD, with the wavelets providing refinement to this representation. The MRTD with Haar wavelets is therefore a natural extension of the traditional FDTD, thereby constituting a good starting point for MRTD consideration. One can show, for example, that Haar-based MRTD with  $n$  wavelet levels is equivalent to FDTD with an expansion in terms of pulses  $1/2^n$  the width of the Haar scaling function. One might consequently argue that Haar-based MRTD and FDTD are equivalent. The difference

Manuscript received September 11, 2000; revised February 9, 2001. This work was supported by the U.S. Army Research Office under Grant DAAD19-99-1-0192.

The authors are with the Department of Electrical and Computer Engineering, Duke University, Durham, NC 27708-0291 USA.

Publisher Item Identifier S 0018-926X(01)09192-X.

is manifested when one realizes that the MRTD offers significantly more flexibility than FDTD. In particular, in the MRTD, one need not use the same number of wavelet levels throughout the computational domain. In regions of relatively slow spatial field variation, one can use scaling functions alone. Where fields vary more quickly, successively higher wavelet levels can be added. Consequently, in the context of a Haar-based MRTD, one effectively realizes a natural multiscale gridding of the traditional FDTD. There has been previous work on the development of multiscale FDTD gridding schemes, although in that work there have been issues regarding algorithmic stability [12]–[14], which is not a problem for the MRTD.

As discussed further in Section II, other advantages of the MRTD are found in the natural way in which general material interfaces and heterogeneity are handled, without the need for a staircase interface approximation, or the introduction of special conformal interface cells. As with the multiscale gridding discussed above, authors have developed techniques for improved accommodation of general material interfaces within the FDTD [15]. The point is not that general interfaces cannot be handled via FDTD, but rather that such issues are treated naturally and easily within the MRTD construct [8], [9]. We also reiterate that the basic MRTD is applicable to a general wavelet expansion, not only the simple Haar wavelets [8], [9], [11] considered here, and further benefits are manifested in the reduced MRTD numerical dispersion with smooth wavelets, *vis-à-vis* the traditional FDTD [9].

Previous published work with MRTD has focused primarily on its application to high-speed integrated circuits [8], [9]. There has recently been investigation of two-dimensional electromagnetic scattering via MRTD, with primary focus on interaction with rough interfaces [16]. It is believed that this paper constitutes the first fully three-dimensional analysis of electromagnetic scattering with MRTD, with the principal focus here on subsurface sensing, although free-space scattering examples are also presented as a special case.

The remainder of this paper is organized as follows. In Section II, we present a detailed discussion of the MRTD scattering formalism, with an implementation in terms of Haar wavelets. We consider plane-wave excitation and therefore discuss extension of the traditional FDTD connecting surface to the MRTD problem. We also discuss MRTD implementation of the perfectly matched layer (PML) absorbing boundary condition. Several example results are presented in Section III, with the MRTD data compared to results computed via an independent MoM solution and to FDTD-generated data. Conclusions and future directions are discussed in Section IV.

## II. MRTD SCATTERING FORMULATION

### A. Basic Formulation

We begin the MRTD analysis by expanding the electromagnetic fields in terms of a wavelet basis, composed of scaling and wavelet functions, in a manner analogous to the well-known method of moments [3], [4]. Scaling functions are employed in regions characterized by smoothly varying fields (coarse field representation), while additional sampling points (refinement) are introduced by incorporating wavelets in regions of fast field

variation. This yields a natural multiresolution field representation.

In the results presented subsequently, comparisons are made between MRTD and FDTD results [2], [7], [15]. The FDTD can be viewed as a field expansion in terms of pulse basis functions (cubes in three dimensions), these pulses being analogous to the Haar scaling function. Haar wavelets therefore represent a good starting point for examination of MRTD. Let the Haar scaling function be represented by  $\phi$ , with the mother wavelet denoted  $\psi$ . These functions are depicted in Fig. 1. Although a wavelet decomposition can be performed in time as well, here the time variation is expanded in a pulse basis  $h$ . Assuming an expansion in terms of scaling functions and a single level of wavelets, we have

$$\begin{aligned}
 F(x, y, z, t) = & \sum_{i,j,k,m=-\infty}^{\infty} h_{m+\delta t}(t) \\
 & \times \left[ F_{i,j,k}^{\phi,\phi,\phi} \phi_{i+\delta x}(x) \phi_{j+\delta y}(y) \phi_{k+\delta z}(z) \right. \\
 & + F_{i,j,k}^{\phi,\phi,\psi} \phi_{i+\delta x}(x) \phi_{j+\delta y}(y) \psi_{k+\delta z}(z) \\
 & + F_{i,j,k}^{\phi,\psi,\phi} \phi_{i+\delta x}(x) \psi_{j+\delta y}(y) \phi_{k+\delta z}(z) \\
 & + F_{i,j,k}^{\phi,\psi,\psi} \phi_{i+\delta x}(x) \psi_{j+\delta y}(y) \psi_{k+\delta z}(z) \\
 & + F_{i,j,k}^{\psi,\phi,\phi} \psi_{i+\delta x}(x) \phi_{j+\delta y}(y) \phi_{k+\delta z}(z) \\
 & + F_{i,j,k}^{\psi,\phi,\psi} \psi_{i+\delta x}(x) \phi_{j+\delta y}(y) \psi_{k+\delta z}(z) \\
 & + F_{i,j,k}^{\psi,\psi,\phi} \psi_{i+\delta x}(x) \psi_{j+\delta y}(y) \phi_{k+\delta z}(z) \\
 & \left. + F_{i,j,k}^{\psi,\psi,\psi} \psi_{i+\delta x}(x) \psi_{j+\delta y}(y) \psi_{k+\delta z}(z) \right] \quad (1)
 \end{aligned}$$

where  $F$  denotes any electric or magnetic field component. The indexes  $i, j, k$ , and  $m$  are the discrete space and time indexes related to the space and time coordinates, analogous to the traditional FDTD [2],[7],[15], with  $\delta x, \delta y, \delta z$ , and  $\delta t$  representing displacements along the  $x, y, z$ , and  $t$  directions. Table I summarizes the relative shifts between the different field components, constituting the MRTD unit cell, assuming Haar expansion with scaling functions and a single level of wavelets.

Considering (1) more closely, we note that each field component is represented by eight terms (e.g.,  $\phi(x)\phi(y)\phi(z)$ ,  $\phi(x)\phi(y)\psi(z)$ , etc.), each of which is a three-dimensional basis function realized here in terms of a Haar scaling function and a single wavelet level. The eight basis functions are analogous to taking a single FDTD cubic basis and dividing it in half in three dimensions, yielding eight smaller cubes where there was one. In general, a single scaling function plus  $n$  wavelet levels will produce  $8^n$  basis functions per unit cell, for a given field component, which is equivalent to FDTD with  $8^n$  cubes within the volume of the scaling functions alone. As discussed further below, by selectively pruning the number of wavelets utilized in a given region, one can realize a multigrid FDTD scheme without the stability concerns of previous multigrid FDTD algorithms [12]–[14]. We also note from (1) and Table I that the  $8^n$  basis functions used to represent *different* field components are in general shifted spatially by a quarter-cell with respect to one another (a cell corresponding to the size of the scaling function), analogous to FDTD in which the different field

TABLE I  
DISPLACEMENTS FOR DIFFERENT FIELD COMPONENTS

	$E_x$	$E_y$	$E_z$	$H_x$	$H_y$	$H_z$
$\delta x(\text{cells})$	0.25	0	0	0	0.25	0.25
$\delta y(\text{cells})$	0	0.25	0	0.25	0	0.25
$\delta z(\text{cells})$	0	0	0.25	0.25	0.25	0
$\delta t(\Delta t)$	0	0	0	0.5	0.5	0.5

components are in general also shifted in space with respect to one another [2], [7], [15]. However, in FDTD, the shift is by half a cell.

Consider a homogeneous medium with electric permittivity  $\epsilon$ , magnetic permeability  $\mu$ , and conductivity  $\sigma$ . An example equation from Ampere's law can be expressed in Cartesian coordinates as

$$\frac{\partial H_z}{\partial y} - \frac{\partial H_y}{\partial z} = \epsilon \frac{\partial E_x}{\partial t} + \sigma E_x. \quad (2)$$

Inserting (1) in (2), we obtain the MRTD equations by employing a Galerkin's testing procedure [4], with the subsequent difference-equation representative of (2) given as

$$[E_x]_{i,j,k}^{(m+1)} = \alpha [E_x]_{i,j,k}^{(m)} + \beta \left\{ \begin{aligned} & \left( [C_1][H_z]_{i,j,k}^{(m)} - [C_2][H_z]_{i,j-1,k}^{(m)} \right) \\ & - \left( [D_1][H_y]_{i,j,k}^{(m)} - [D_2][H_y]_{i,j,k-1}^{(m)} \right) \end{aligned} \right\} \quad (3)$$

where the space discretization (size of the scaling function) in the  $x$ -,  $y$ -, and  $z$ -directions is assumed to be the same. The constants  $\alpha = (1 - (\sigma\Delta t/2\epsilon))/(1 + (\sigma\Delta t/2\epsilon))$  and  $\beta = \Delta t/(\epsilon\Delta x(1 + \sigma\Delta t/2\epsilon))$  corresponded to the material characteristics of the cell. The vector  $[E_x]_{i,j,k}$  represents the eight basis functions discussed above, for the field component  $E_x$  at the discrete spatial coordinates  $(i, j, k)$ , with the superscripts in (3) representing the discrete time index  $m$ , as in the FDTD. The eight components of the fields are arranged as shown in (4) at the bottom of the page for  $E_x$ , and the matrices are

$$[C_1] = \begin{bmatrix} 1 & 0 & -1 & 0 & 0 & 0 & 0 & 0 \\ 0 & 1 & 0 & -1 & 0 & 0 & 0 & 0 \\ 1 & 0 & 3 & 0 & 0 & 0 & 0 & 0 \\ 0 & 1 & 0 & 3 & 0 & 0 & 0 & 0 \\ 0 & 0 & 0 & 0 & 1 & 0 & -1 & 0 \\ 0 & 0 & 0 & 0 & 0 & 1 & 0 & -1 \\ 0 & 0 & 0 & 0 & 1 & 0 & 3 & 0 \\ 0 & 0 & 0 & 0 & 0 & 1 & 0 & 3 \end{bmatrix} \quad (5a)$$

$$[C_2] = \begin{bmatrix} 1 & 0 & -1 & 0 & 0 & 0 & 0 & 0 \\ 0 & 1 & 0 & -1 & 0 & 0 & 0 & 0 \\ 1 & 0 & -1 & 0 & 0 & 0 & 0 & 0 \\ 0 & 1 & 0 & -1 & 0 & 0 & 0 & 0 \\ 0 & 0 & 0 & 0 & 1 & 0 & -1 & 0 \\ 0 & 0 & 0 & 0 & 0 & 1 & 0 & -1 \\ 0 & 0 & 0 & 0 & 1 & 0 & -1 & 0 \\ 0 & 0 & 0 & 0 & 0 & 1 & 0 & -1 \end{bmatrix} \quad (5b)$$

$$[D_1] = \begin{bmatrix} 1 & -1 & 0 & 0 & 0 & 0 & 0 & 0 \\ 1 & 3 & 0 & 0 & 0 & 0 & 0 & 0 \\ 0 & 0 & 1 & -1 & 0 & 0 & 0 & 0 \\ 0 & 0 & 1 & 3 & 0 & 0 & 0 & 0 \\ 0 & 0 & 0 & 0 & 1 & -1 & 0 & 0 \\ 0 & 0 & 0 & 0 & 1 & 3 & 0 & 0 \\ 0 & 0 & 0 & 0 & 0 & 0 & 1 & -1 \\ 0 & 0 & 0 & 0 & 0 & 0 & 1 & 3 \end{bmatrix} \quad (5c)$$

$$[D_2] = \begin{bmatrix} 1 & -1 & 0 & 0 & 0 & 0 & 0 & 0 \\ 1 & -1 & 0 & 0 & 0 & 0 & 0 & 0 \\ 0 & 0 & 1 & -1 & 0 & 0 & 0 & 0 \\ 0 & 0 & 1 & -1 & 0 & 0 & 0 & 0 \\ 0 & 0 & 0 & 0 & 1 & -1 & 0 & 0 \\ 0 & 0 & 0 & 0 & 1 & -1 & 0 & 0 \\ 0 & 0 & 0 & 0 & 0 & 0 & 1 & -1 \\ 0 & 0 & 0 & 0 & 0 & 0 & 1 & -1 \end{bmatrix} \quad (5d)$$

with these found through the testing procedure and via the relations

$$\int \psi_{i+1/4}(x) \phi_i(x) dx = 0 \quad (6a)$$

$$\int \frac{\partial \phi_{i+1/4}(x)}{\partial x} \phi_i(x) dx = \delta_{i,i} - \delta_{i-1,i} \quad (6b)$$

$$\int \frac{\partial \psi_{i+1/4}(x)}{\partial x} \phi_i(x) dx = \delta_{i-1,i} - \delta_{i,i} \quad (6c)$$

$$\int \frac{\partial \phi_{i+1/4}(x)}{\partial x} \psi_i(x) dx = \delta_{i,i} - \delta_{i-1,i} \quad (6d)$$

$$\int \frac{\partial \psi_{i+1/4}(x)}{\partial x} \psi_i(x) dx = \delta_{i-1,i} + 3\delta_{i,i} \quad (6e)$$

where  $\delta_{i,j} = 1$  if  $i = j$  and  $\delta_{i,j} = 0$  if  $i \neq j$ . The MRTD equations for the other field components can be deduced similarly.

$$[E_x]_{i,j,k} = [E_x^{\phi,\phi,\phi} \quad E_x^{\phi,\phi,\psi} \quad E_x^{\phi,\psi,\phi} \quad E_x^{\phi,\psi,\psi} \quad E_x^{\psi,\phi,\phi} \quad E_x^{\psi,\phi,\psi} \quad E_x^{\psi,\psi,\phi} \quad E_x^{\psi,\psi,\psi}]_{i,j,k}^T \quad (4)$$

The matrix-based representation of the update (3)–(5) constitutes a compact MRTD implementation and is applicable to a general wavelet basis and an arbitrary number of wavelet levels. If higher order wavelet levels are considered, the matrices increase in size. Through consideration of the integrals in (6), it also clear that wavelets and scaling functions of compact support are desirable, such that the matrices in (3)–(5) are as small as possible.

In (3)–(5), scaling and wavelet functions are used throughout the computational domain. As discussed in Section III, in practice scaling functions are used everywhere and wavelets are only utilized in regions of relatively fast field variation. In the results presented below, we consider regions that are represented in terms of scaling functions alone, for each of the three dimensions, and other regions in which spatial variation in each Cartesian direction is expanded in terms of scaling functions and a single wavelet level. This implies that in some regions, one basis function is used within the volume of the three-dimensional scaling function (scaling functions alone), and in other regions, eight basis functions are used (scaling function plus single wavelet level). This is analogous to a multigrid FDTD scheme [12]–[14], in which a certain cubic basis is used in some regions and, in other regions, eight smaller cubes are used in this same volume. However, we note that within the context of MRTD, we need not restrict ourselves to one or eight basis functions within a given cubic volume. We can utilize a subset of the components in (4), ranging from one to eight. For example, if we apply wavelets in the  $x$ - and  $y$ -directions, but only scaling functions in  $z$ , we realize bases that are analogous to FDTD with *noncubic* basis functions (the basis length in  $z$  is twice that in  $x$  and  $y$ ). This is appropriate for geometries in which the fields may vary quickly in  $x$  and  $y$ , but not in  $z$ . We do not consider this higher level pruning scheme here, but this discussion points out the flexibility of MRTD, even with simple Haar basis functions.

With regard to the stability condition, as indicated in the Introduction, a Haar-based MRTD with  $n$  wavelet levels, assuming a scaling function of width  $w$ , is identical to an FDTD scheme with spatial sampling of  $w/2^n$ , and therefore the Haar-based MRTD stability condition can be easily borrowed from that of the traditional FDTD [2], [7], [15]. We note that for a more general wavelet expansion, the stability condition is different than that of the FDTD [9]. Finally, as in the FDTD analysis, one need

only store the time-dependent basis-function coefficients on a Huygen's surface enclosing the target. The scattered fields at any position outside the Huygen surface are calculated by convolving the Huygen equivalent currents with the Green's function characteristic of the outside region.

### B. Dielectric Interfaces

The surfaces of arbitrary-shaped dielectric objects are generally not conformal to the Haar-MRTD rectangular grid. Similar issues occur in the FDTD, in which one can consider a staircase approximation to the interface [17], averaging [15], or conformal FDTD cells [18]. While conformal FDTD cells can be tailored to general surfaces, the mesh for each target must be considered anew. Within the context of MRTD, there are no such issues. The same wavelet-based mesh is applied to all inhomogeneities, without requiring a staircase approximation. Again considering (2), for example, the wavelet expansion and Galerkin testing yield a generalized form of (3), expressed as

$$\begin{aligned} & \left( \frac{1}{\Delta t} [\varepsilon]_{i,j,k} + \frac{1}{2} [\sigma]_{i,j,k} \right) [E_x]_{i,j,k}^{(m+1)} \\ & - \left( \frac{1}{\Delta t} [\varepsilon]_{i,j,k} - \frac{1}{2} [\sigma]_{i,j,k} \right) [E_x]_{i,j,k}^{(m)} \\ & = \frac{1}{\Delta x} \left\{ ([C_1][H_z]_{i,j,k}^{(m)} - [C_2][H_z]_{i,j,k-1}^{(m)}) \right. \\ & \quad \left. - ([D_1][H_y]_{i,j,k}^{(m)} - [D_2][H_y]_{i,j,k-1}^{(m)}) \right\} \quad (7) \end{aligned}$$

where we have (8), shown at the bottom of the page. We observe that there are only eight elements required in (8), expressed as

$$\varepsilon_{i,j,k}^{\chi,\xi,\zeta} = \frac{1}{\Delta x^3} \iiint_{\text{cell } i,j,k} \varepsilon(x,y,z) \phi_{i+\delta x}(x) \phi_{j+\delta y}(y) \phi_{k+\delta z}(z) \chi_{i+\delta x}(x) \xi_{j+\delta y}(y) \zeta_{k+\delta z}(z) dx dy dz \quad (9)$$

where  $\varepsilon(x,y,z)$  is the distribution function of the permittivity and  $\chi$ ,  $\xi$ , and  $\zeta$  can be function  $\phi$  or  $\psi$ . We also obtain the analogous matrix  $[\sigma]_{i,j,k}$ . From (7), we see that the inverse of  $((1/\Delta t)[\varepsilon] + (1/2)[\sigma])$  is required for each cell filled with inhomogeneous media to obtain an explicit updating equation. This is not a big burden since all matrices are computed once and subsequently utilized in the time-stepping algorithm. Moreover,

$$[\varepsilon]_{i,j,k} = \begin{bmatrix} \varepsilon_{i,j,k}^{\phi,\phi,\phi} & \varepsilon_{i,j,k}^{\phi,\phi,\psi} & \varepsilon_{i,j,k}^{\phi,\psi,\phi} & \varepsilon_{i,j,k}^{\phi,\psi,\psi} & \varepsilon_{i,j,k}^{\psi,\phi,\phi} & \varepsilon_{i,j,k}^{\psi,\phi,\psi} & \varepsilon_{i,j,k}^{\psi,\psi,\phi} & \varepsilon_{i,j,k}^{\psi,\psi,\psi} \\ \varepsilon_{i,j,k}^{\phi,\psi,\phi} & \varepsilon_{i,j,k}^{\phi,\psi,\psi} & \varepsilon_{i,j,k}^{\psi,\phi,\phi} & \varepsilon_{i,j,k}^{\psi,\phi,\psi} & \varepsilon_{i,j,k}^{\psi,\psi,\phi} & \varepsilon_{i,j,k}^{\psi,\psi,\psi} & \varepsilon_{i,j,k}^{\psi,\psi,\phi} & \varepsilon_{i,j,k}^{\psi,\psi,\psi} \\ \varepsilon_{i,j,k}^{\psi,\phi,\phi} & \varepsilon_{i,j,k}^{\psi,\phi,\psi} & \varepsilon_{i,j,k}^{\psi,\psi,\phi} & \varepsilon_{i,j,k}^{\psi,\psi,\psi} & \varepsilon_{i,j,k}^{\psi,\psi,\phi} & \varepsilon_{i,j,k}^{\psi,\psi,\psi} & \varepsilon_{i,j,k}^{\psi,\psi,\phi} & \varepsilon_{i,j,k}^{\psi,\psi,\psi} \\ \varepsilon_{i,j,k}^{\psi,\psi,\phi} & \varepsilon_{i,j,k}^{\psi,\psi,\psi} & \varepsilon_{i,j,k}^{\psi,\psi,\phi} & \varepsilon_{i,j,k}^{\psi,\psi,\psi} & \varepsilon_{i,j,k}^{\psi,\psi,\phi} & \varepsilon_{i,j,k}^{\psi,\psi,\psi} & \varepsilon_{i,j,k}^{\psi,\psi,\phi} & \varepsilon_{i,j,k}^{\psi,\psi,\psi} \\ \varepsilon_{i,j,k}^{\psi,\psi,\phi} & \varepsilon_{i,j,k}^{\psi,\psi,\psi} & \varepsilon_{i,j,k}^{\psi,\psi,\phi} & \varepsilon_{i,j,k}^{\psi,\psi,\psi} & \varepsilon_{i,j,k}^{\psi,\psi,\phi} & \varepsilon_{i,j,k}^{\psi,\psi,\psi} & \varepsilon_{i,j,k}^{\psi,\psi,\phi} & \varepsilon_{i,j,k}^{\psi,\psi,\psi} \\ \varepsilon_{i,j,k}^{\psi,\psi,\phi} & \varepsilon_{i,j,k}^{\psi,\psi,\psi} & \varepsilon_{i,j,k}^{\psi,\psi,\phi} & \varepsilon_{i,j,k}^{\psi,\psi,\psi} & \varepsilon_{i,j,k}^{\psi,\psi,\phi} & \varepsilon_{i,j,k}^{\psi,\psi,\psi} & \varepsilon_{i,j,k}^{\psi,\psi,\phi} & \varepsilon_{i,j,k}^{\psi,\psi,\psi} \\ \varepsilon_{i,j,k}^{\psi,\psi,\phi} & \varepsilon_{i,j,k}^{\psi,\psi,\psi} & \varepsilon_{i,j,k}^{\psi,\psi,\phi} & \varepsilon_{i,j,k}^{\psi,\psi,\psi} & \varepsilon_{i,j,k}^{\psi,\psi,\phi} & \varepsilon_{i,j,k}^{\psi,\psi,\psi} & \varepsilon_{i,j,k}^{\psi,\psi,\phi} & \varepsilon_{i,j,k}^{\psi,\psi,\psi} \end{bmatrix}. \quad (8)$$

the matrixes  $[\varepsilon]_{i,j,k}$  and  $[\sigma]_{i,j,k}$  are diagonal if the cell  $(i, j, k)$  is homogeneous. For this case, (7) reduces to (3). Therefore, we only use the form in (7) for cells in which the material is inhomogeneous.

### C. Connecting Surface

When the source is distant from the target of interest, the incident fields can typically be well approximated in terms of a plane wave. We here employ a connecting surface [15], which divides the fields into total fields (inside surface) and scattered fields (outside surface). Connecting surfaces have been discussed previously in the context of FDTD, and here they are discussed in terms of MRTD. To implement a connecting surface, one requires the time-domain incident plane-wave fields on a closed surface enclosing the target. For free-space scattering, these fields can be expressed in closed form, while for more general media, more care is required. In particular, in the context of subsurface sensing, one is interested in a pulsed plane wave incident in the presence of a lossy half-space [3], [4], [6]. For this problem, the incident fields are frequency dependent, and therefore they are calculated in closed form in the frequency domain, with the time-domain incident fields on the connecting surface synthesized via Fourier transform. Note that in the half-space in which the incident fields first arrive, the incident fields due to an infinite half-space include the initial incident fields plus the Snell's-law reflected component, while in the subsurface the incident fields are represented by the transmitted component.

For the cells in the vicinity of the connecting surface, the update equations, e.g., (3) and (7), contain both total- and scattered-field terms. Correction terms are introduced to balance this disparity, with the terms represented by the incident fields [15]. We again consider (3), for example. For MRTD cells around the connecting surface, the fields on one side of the surface are scattered fields alone and on the other side total fields. Consider the bottom of a connecting surface, with  $z$ -position  $k$  in the total field region and  $k-1$  in the scattered-field region. The coefficients  $H_{y_{i,j,k-1}}^{\phi,\phi,\phi}$  and  $H_{y_{i,j,k-1}}^{\phi,\phi,\psi}$  are related to the scattered-field region, while the other coefficients are related to the total-field region. Therefore, to keep the equation consistent, a correction term  $E_{x_{i,j,k}}^{\phi,\phi,\phi(m+1)}|_{\text{correction}}$  is added on the right side of (3). In this case, the correction  $E_{x_{i,j,k}}^{\phi,\phi,\phi(m+1)}|_{\text{correction}}$  is expressed as

$$E_{x_{i,j,k}}^{\phi,\phi,\phi(m+1)}|_{\text{correction}} = \beta \left[ H_{y_{i,j,k-1}}^{\phi,\phi,\phi(m)}|_{\text{incident}} - H_{y_{i,j,k-1}}^{\phi,\phi,\psi(m)}|_{\text{incident}} \right] \quad (10)$$

We see therefore that the correction terms in the MRTD are handled analogously to how they are treated in the FDTD.

### D. Perfectly Matched Layer (PML)

A PML [19], [20] is employed as the absorbing boundary conditions. To save computer memory, we only split the fields [19] in the PML region. We again consider  $E_x$  as an example. This field component can be split into two parts,  $E_{xy}$  and  $E_{xz}$  [19], which propagate along the  $y$ - and  $z$ -direction, respectively.

The corresponding governing equations for lossy medium are therefore expressed as

$$\varepsilon \frac{\partial E_{xy}}{s_0 \partial t} + (\sigma + \sigma_y) E_{xy} + \frac{\sigma \sigma_y}{\varepsilon} \varsigma_{xy} = \frac{\partial H_z}{\partial y} \quad (11a)$$

$$\varepsilon \frac{\partial E_{xz}}{s_0 \partial t} + (\sigma + \sigma_z) E_{xz} + \frac{\sigma \sigma_z}{\varepsilon} \varsigma_{xz} = - \frac{\partial H_y}{\partial z} \quad (11b)$$

$$\frac{\partial \varsigma_{xy}}{\partial t} = E_{xy} \quad (11c)$$

$$\frac{\partial \varsigma_{xz}}{\partial t} = E_{xz} \quad (11d)$$

where  $\varsigma_{xy}$  and  $\varsigma_{xz}$  are two auxiliary variables, and the appropriate selection of the parameters  $s_0$ ,  $\sigma_y$ , and  $\sigma_z$  can be found in [20]. The corresponding MRTD updating equations are now rewritten as

$$[E_{xy}]_{i,j,k}^{(m+1)} = \alpha_{xy} [E_{xy}]_{i,j,k}^{(m)} + \beta_{xy} \left( [C_1] [H_z]_{i,j,k}^{(m)} - [C_2] [H_z]_{i,j-1,k}^{(m)} \right) - s_0 \frac{\sigma \sigma_y}{\varepsilon} E_{xy}^{(m)} \quad (12a)$$

$$[E_{xz}]_{i,j,k}^{(m+1)} = \alpha_{xz} [E_{xz}]_{i,j,k}^{(m)} - \beta_{xz} \left( [D_1] [H_y]_{i,j,k}^{(m)} - [D_2] [H_y]_{i,j,k-1}^{(m)} \right) - s_0 \frac{\sigma \sigma_z}{\varepsilon} E_{xz}^{(m)} \quad (12b)$$

where the coefficients  $\alpha_v$  and  $\beta_v$  (index  $v$  can be  $xy$  or  $xz$ ) are given by

$$\alpha_v = \frac{1}{s_0} \exp \left( - \frac{(\sigma + \sigma_y, \text{or } z) \Delta t}{\varepsilon} \right) \quad (13a)$$

$$\beta_v = \frac{1}{s_0} \frac{1 - \exp \left( - \frac{(\sigma + \sigma_y, \text{or } z) \Delta t}{\varepsilon} \right)}{\sigma \Delta x} \quad (13b)$$

where the exponential time-stepping [19] has been used. Consequently, like the connecting surface, the PML is handled in a manner analogous to FDTD [19].

## III. RESULTS

Several scattering scenarios are presented for dielectric targets in vacuum as well as targets in the vicinity of a lossy half-space, the latter motivated by subsurface-sensing applications. The examples are selected to underscore the strengths and limitations of the MRTD, as implemented via Haar wavelets. In all examples, plane-wave excitation is considered, with connecting-surface implementation as discussed in Section II.C.

### A. Dielectric Sphere in Free Space

We first consider a lossless dielectric sphere of relative permittivity  $\epsilon_r = 4$  and 16 cm radius, in free space, with results compared with data calculated via an MoM analysis tailored for a body of revolution (BoR) [21]. The comparison is performed in terms of radar cross section (RCS) as a function of frequency. Concerning the MRTD results, a Fourier transform is taken of the time-domain fields on the surface of a Huygen's surface that

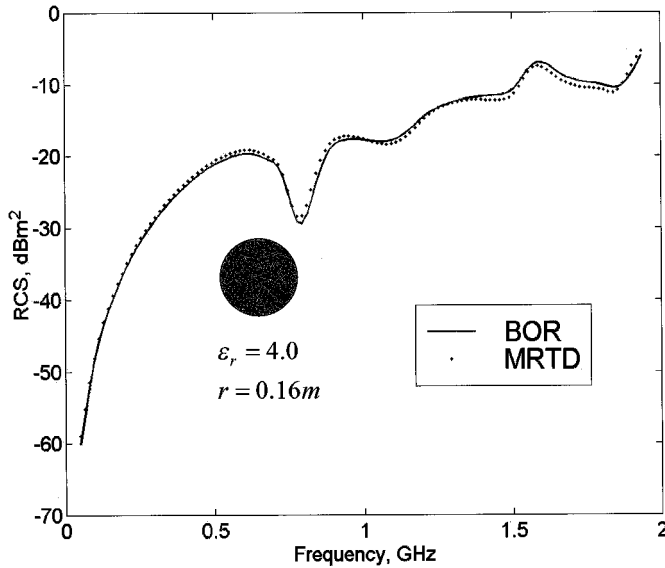


Fig. 2. Monostatic RCS of a 16-cm-radius dielectric sphere of dielectric constant;  $\epsilon_r = 4$ , as computed via MRTD and a BoR-MoM model [21].

encloses the target, with these frequency-domain fields spatially convolved with the appropriate Green's function, to compute the far-zone scattered fields. These fields are then divided by the frequency response of the incident waveform to deconvolve the effects of the incident pulse. In this example, we use the free-space Green's function; in examples below, the half-space Green's function is employed. We see in Fig. 2 that the agreement between the frequency-dependent MRTD and BoR-MoM results is generally good. In this example, the PML is placed 4 cm from the surface of the sphere, and therefore almost the entire computational domain is occupied by the target. Consequently, for this example, we do not exploit the multiresolution properties of MRTD, since the air region outside the target is a very small fraction of the target volume. In particular, there is little computational savings in using scaling functions alone in the air region (outside the target) and scaling functions and wavelets inside the target. Therefore, the Haar scaling function and a single level of wavelets are used throughout.

In this example, the principal advantage of the MRTD is manifested in the analysis of the curved spherical surface, which is not matched to a Cartesian lattice. In particular, we have used both scaling functions and wavelets throughout the computational domain, with the smallest dimension cubes in this analysis having a volume of  $1 \times 1 \times 1 \text{ cm}^3$ , which constitutes a relatively coarse representation for the sphere considered (an FDTD staircase approximation with this discretization yields errors on the order of 2.0 dB). Within the context of MRTD, the inhomogeneity is handled as discussed in Section II-B.

### B. Two Dielectric Cylinders in Free Space

The example in Section III-A underscores that not all targets necessarily require a multiresolution algorithm. However, there are many complex targets for which such an analysis is particularly useful. As such an example, we consider the bistatic RCS from two proximate dielectric cylinders in free space. The scattering geometry is shown in Fig. 3, with dimensions  $D_1 = 20 \text{ cm}$ ,  $D_2 = 12 \text{ cm}$ ,  $h_1 = 102 \text{ cm}$ ,  $h_2 = 42 \text{ cm}$ , and  $l =$

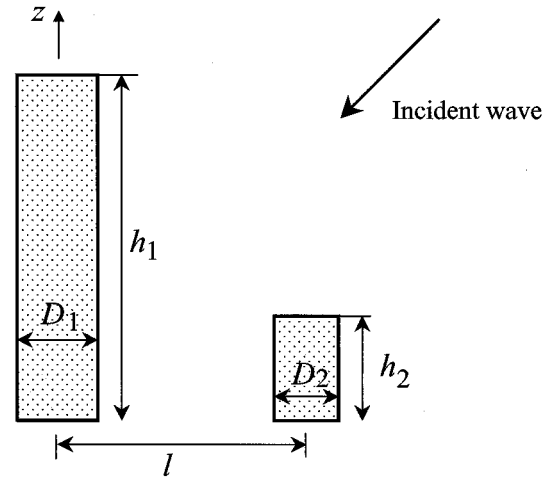


Fig. 3. Two dielectric cylinders in free space with plane-wave excitation.

80 cm. The relative permittivity of each target is  $\epsilon_r = 3$ . In Fig. 4, we compare the bistatic RCS as computed via MRTD and FDTD, for a frequency of 700 MHz, with incident angles  $\theta_{\text{inc}} = 45^\circ$  and  $\varphi_{\text{inc}} = 0^\circ$ , with observation at the angles  $\theta_s = 90^\circ$  and  $\varphi_s = 0 - 180^\circ$ . While one is unlikely to perform such a bistatic measurement in practice, we have found bistatic comparisons to be a particularly good test of model accuracy. The frequency-domain data are computed from the time-domain MRTD and FDTD fields, as discussed in Section III-A.

In the FDTD computations, a cell size of  $1 \times 1 \times 1 \text{ cm}^3$  is used throughout. In the MRTD computations, wavelets are used in the vicinity of the targets, with scaling functions alone used outside. Where wavelets are employed, the resolution is as in the FDTD, and in the regions of scaling functions alone the sampling is half as fine (one MRTD cube, where FDTD employs eight). In the vicinity of the connecting surface, for the incident fields, both scaling functions and wavelets are used. For the FDTD computations the material interface at the target surface is treated via averaging the respective permittivities [15], while in the MRTD the material inhomogeneity is handled as discussed in Section II-B. We consider the copolarized fields in Fig. 4(a) and the cross-polarized case in Fig. 4(b). We see that the agreement between the FDTD and MRTD computations is generally good.

For the computations considered in Fig. 4, 28% of the MRTD volume is modeled via scaling functions alone, with the remainder modeled via a single level of wavelets as well. In the time-domain computations, a fourth-order Rayleigh pulse [22] (central frequency is 600 MHz) is chosen as the source, and the MRTD calculations required 23% less computation time (CPU) *vis-à-vis* the FDTD. The savings in computation time is largely dictated by the spatial separation between the two cylinders in Fig. 3, with further advantages of MRTD realized as this separation is increased.

### C. Canonical Buried Targets

Many land mines are cylindrical in shape, and with this problem in mind we consider a dielectric cylinder of 4 cm height and 8 cm diameter, with 4 cm between the top of the target and the air-ground interface. The relative permittivity

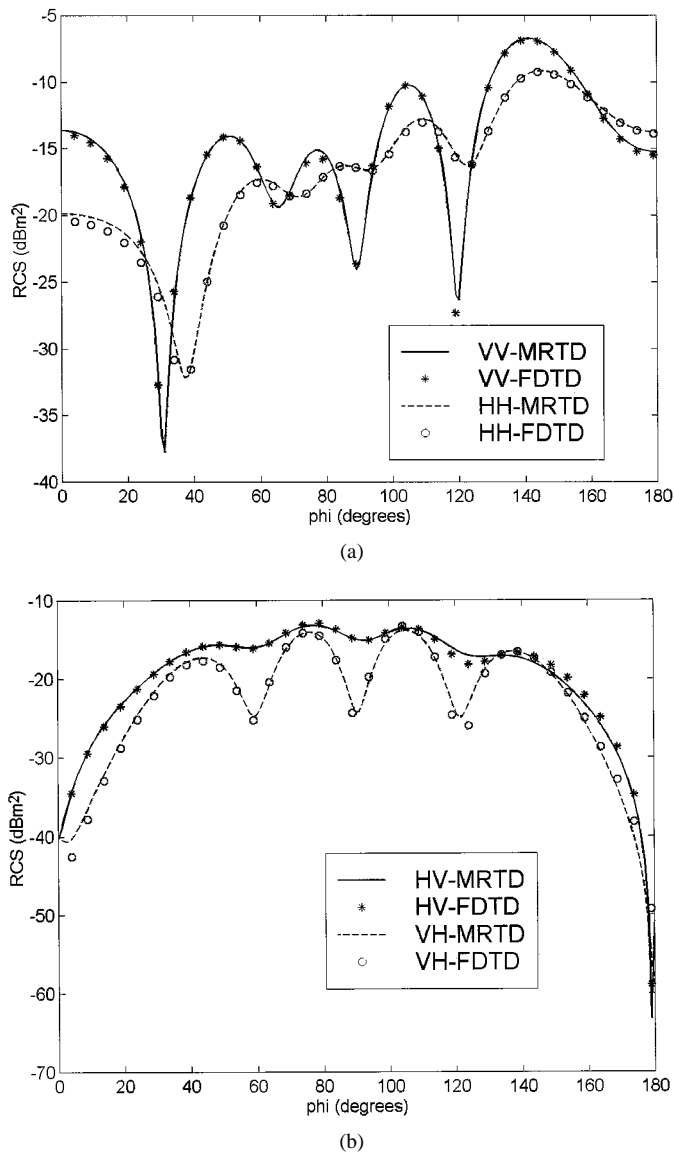


Fig. 4. Bistatic scattering for the target in Fig. 3, at frequency 700 MHz, with  $D_1 = 20$  cm,  $D_2 = 12$  cm,  $h_1 = 102$  cm,  $h_2 = 42$  cm, and  $l = 80$  cm. The relative permittivity of each target is  $\epsilon_r = 3$ . The plane-wave incident angles are  $\theta_{inc} = 45^\circ$  and  $\varphi_{inc} = 0^\circ$ , with observation at the angles  $\theta_s = 90^\circ$  and  $\varphi_s = 0 - 180^\circ$ . The data are computed via MRTD and FDTD. (a) Copolarized and (b) cross-polarized fields.

of the target is  $\epsilon_r = 2$ , and the soil is modeled with a relative permittivity  $\epsilon_r = 5$  and conductivity  $\sigma = 0.01$  S/m. Note that even a real permittivity with frequency-independent conductivity yields a dispersive soil medium. However, often one wishes to employ a more-sophisticated model for the dispersive properties of soil [2]–[4], [6], [7]. Such dispersion has been incorporated into the FDTD formalism [2], [7], and similar modifications can be made to MRTD, although we have not considered such here.

The plane-wave excitation has an incidence angle  $\theta_{inc} = 45^\circ$ , and the bistatic scattered fields are viewed as a function of  $\theta_s$ , in the same azimuthal plane as the incident wave. Results are shown for frequencies of 300, 500, and 700 MHz, with MRTD results compared with data computed via a BoR-MoM model [21]. As indicated in Fig. 5, the bistatic results from these two disparate models are in good relative agreement.

In Fig. 6, we consider the same scattering scenario as in Fig. 5, but now we consider monostatic scattering as a function of frequency. The excitation is incident as in Fig. 4. The agreement between the two models is consistent with our previous examples. In these computations, the PML in the air region is placed close to the air–soil interface, and therefore the air region in these computations constitutes a small percentage of the total computational volume. Moreover, since the target–soil contrast is relatively small, there is less need for a multiresolution analysis. In these MRTD computations, wavelets and scaling functions are employed throughout, with the principal utility of the MRTD again found in the manner by which the curved target surface is handled. The smallest cube in these computations had dimensions  $0.5 \times 0.5 \times 0.5$  cm<sup>3</sup>, and the central frequency of the incident pulse is 900 MHz. Note that in the context of a Haar expansion, when wavelets are used throughout, one could simply utilize scaling functions alone, with cell size split in half (in each dimension).

#### D. Buried Target Near Clutter

As indicated in Section III-D, for many subsurface-sensing problems, the utility of the MRTD multiresolution property is less clear, since the PML allows the air region to be very small (the PML is close to the air–ground interface). In this case, the air region, which permits coarser spatial sampling than the dielectric target and soil, only constitutes a small fraction of the computational domain. However, there are problem classes for which MRTD yields clear advantages. For example, rough-surface scattering is a problem well suited to MRTD, this having been demonstrated previously for two-dimensional problems [16]. In particular, a general rough surface often manifests fine roughness structure that is difficult to model via special conformal FDTD cells [18], due to the generality of the roughness. On the other hand, the natural manner with which MRTD handles dielectric interfaces is well suited to the analysis of such scattering scenarios. Rough-surface scattering is a discipline unto itself and requires a statistical parametrization of the surface and scattered fields [16]. In lieu of addressing this problem directly, we consider a simpler but related scattering scenario. In Fig. 7, we again consider a buried dielectric cylinder, but now there is a protruding bump (“hill”) in the surface, characterized by radius  $r$  and height  $s$ . This bump constitutes one portion of a general rough surface, allowing consideration of relevant numerical issues. In particular, for a “hill” of height  $s$ , assume that  $k$  FDTD cells are employed along the height dimension  $s$  (Fig. 7). As the height  $s$  diminishes, the size of the FDTD cells must diminish ( $k$  must increase). If the FDTD cells are sampled uniformly across the computational domain, as in a traditional FDTD analysis, the accurate representation of this fine structure will significantly increase the numerical size of the problem. Similar issues hold in the context of representing the detail in a rough surface [16].

We consider scattered fields from the situation in Fig. 7, as computed via FDTD and MRTD. In MRTD scaling, functions are used throughout, and a single level of wavelets is used in the subsurface and about the “hill.” Assume that the scaling functions have sides of length  $w$ . In the FDTD analysis, we initially use cells of length  $w/2$ , corresponding to an MRTD

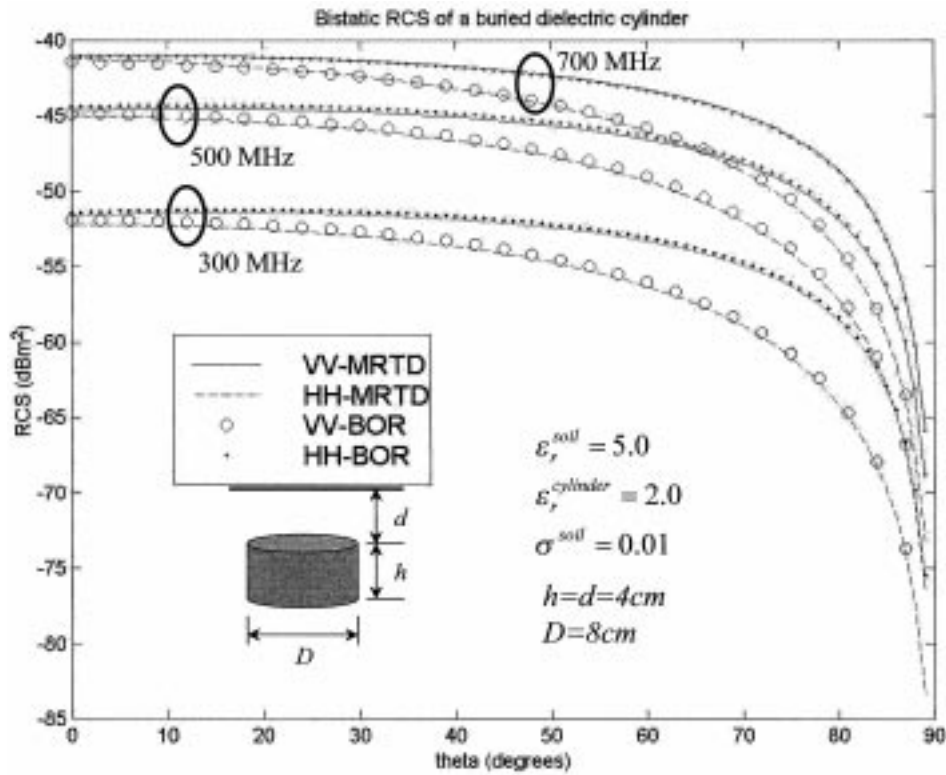


Fig. 5. Copolarized bistatic scattering from a lossless dielectric buried in a lossy half-space (see insert for geometric and electrical parameters). The incident plane wave is incident at  $\theta_{inc} = 45^\circ$ , and the bistatic fields are computed as a function of  $\theta$ , in the same azimuthal plane as the incident wave. Data are computed via the MRTD and BoR-MoM [21] at 300, 500, and 700 MHz.

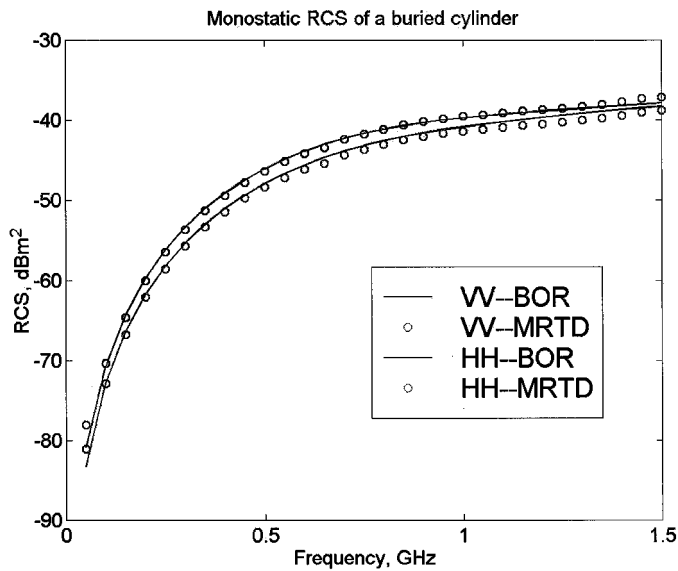


Fig. 6. Monostatic RCS as a function of frequency for the target geometry and incidence angle considered in Fig. 5.

scheme with Haar wavelets throughout. In the MRTD, the “hill” inhomogeneity is modeled as discussed in Section II-B, and the FDTD performs averaging across discrete inhomogeneities [15]. One could also employ conformal FDTD cells [18], but this is not considered here, as this would be difficult to implement for a general rough surface.

The results in Fig. 8 correspond to  $h = 8\text{ cm}$ ,  $d = 4\text{ cm}$ ,  $D = 16\text{ cm}$ ,  $r = 16\text{ cm}$ , and  $l = 30\text{ cm}$  and the relative permittivity

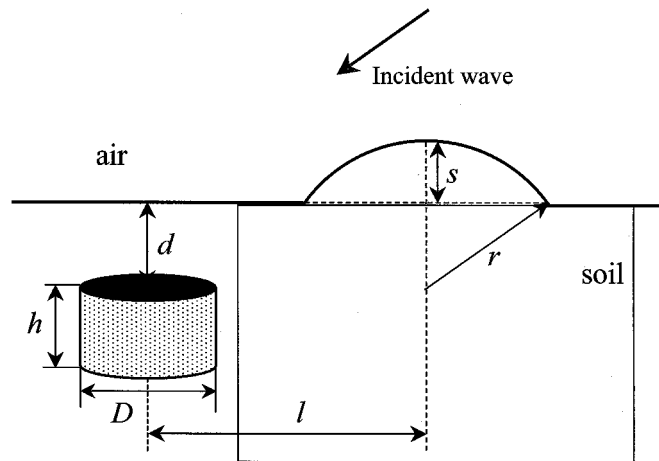


Fig. 7. Scattering geometry for results in Fig. 8 Fig. 9. The plane-wave excitation is incident in the azimuthal plane bisecting the centers of the cylindrical target and spherically shaped surface clutter.

of the lossless target is  $\epsilon_r = 2.0$ . The soil is modeled as in Figs. 5 and 6, and we consider  $s = 3\text{ cm}$ ,  $s = 5\text{ cm}$ , and  $s = 8\text{ cm}$ . In the initial examples, the spatial sampling is  $w = 2\text{ cm}$ , corresponding to  $k = 3$ ,  $k = 5$ , and  $k = 8$  for  $s = 3\text{ cm}$ ,  $s = 5\text{ cm}$  and  $s = 8\text{ cm}$ , respectively. The bistatic RCS is plotted as a function of  $\theta_s$  in a plane bisecting the center of the two scatterers (Fig. 7), with the excitation in this plane at  $\theta_{inc} = 45^\circ$ . As expected, as the size of the hill diminishes, so do the scattered fields. It is also clear that the differences between the MRTD and FDTD increase as the hill size diminishes, which is manifested

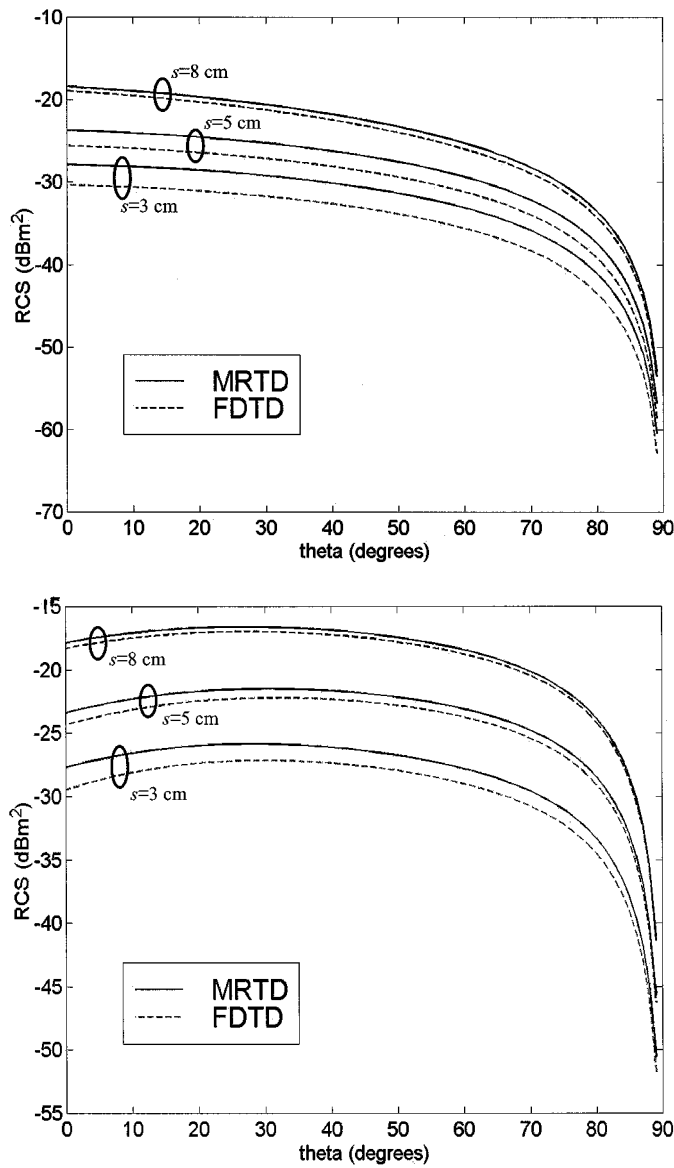


Fig. 8. Bistatic scattering from the target in Fig. 7, with parameters  $h = 8$  cm,  $d = 4$  cm,  $D = 16$  cm,  $r = 16$  cm, and  $l = 30$  cm, and the relative permittivity of the lossless target is  $\epsilon_r = 2.0$ . The soil is modeled as in Figs. 5 and 6, and results are presented for  $s = 3$  cm,  $s = 5$  cm, and  $s = 8$  cm. The plane-wave excitation is at  $\theta_{inc} = 45^\circ$ . The scaling function has a width  $w$  and the FDTD cells have width  $w/2$ , where  $w = 2$  cm. (a) HH polarization and (b) VV polarization.

by the fact that, with the discretization level considered, the hill is not well represented via the FDTD.

In Fig. 9, we again consider the  $s = 3$  cm case but increase the FDTD sample rate. In particular, the FDTD cell width is now  $w/4$ , where  $w$  is again the length of the Haar scaling functions. We see that now the FDTD and MRTD results are in nearly exact agreement for HH polarization and in closer agreement for VV polarization. For the case  $s = 3$  cm,  $k = 3$  in Fig. 8 and  $k = 6$  in Fig. 9. As applied here, a uniform spatial sampling has been used throughout the FDTD model, and therefore the FDTD computations in Fig. 9 required 83% more CPU time than the corresponding MRTD results with scaling-function width  $w$ . A more detailed analysis of the benefits of MRTD for rough-surface scattering is discussed in [16].

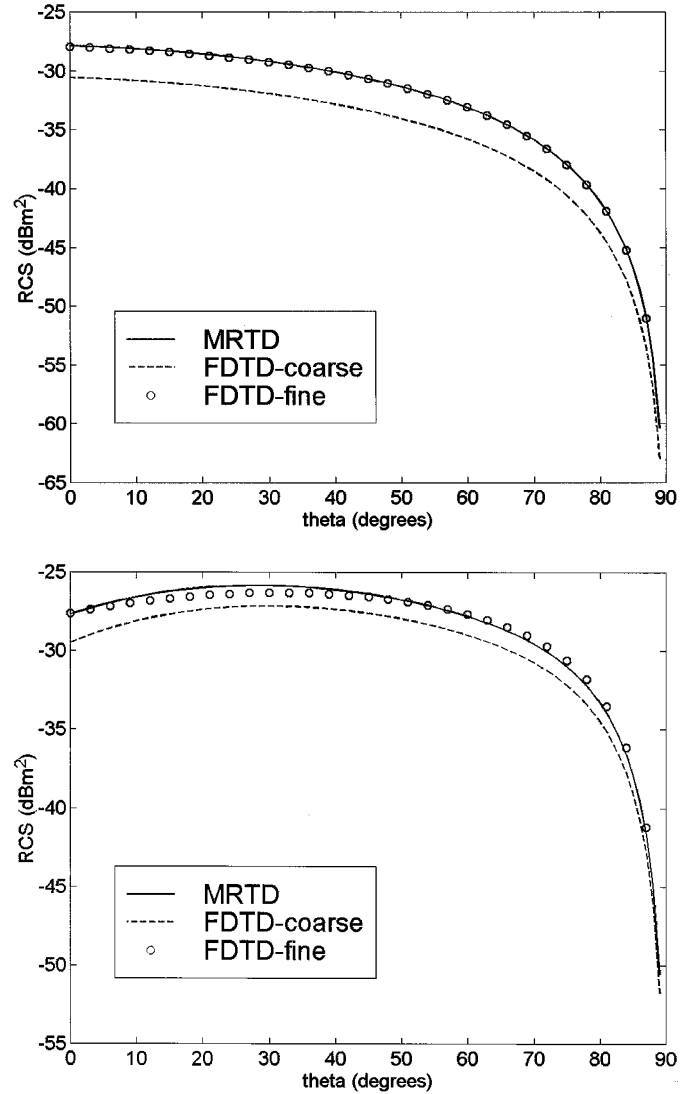


Fig. 9. Bistatic scattering as in Fig. 8, for the case  $s = 3$  cm. The MRTD results are as in Fig. 8, but the FDTD results employ spatial sampling twice as dense as Fig. 8. In particular, the scaling function has a width  $w$  and the FDTD cells have width  $w/4$ , where  $w = 2$  cm. The "coarse" results correspond to data from Fig. 8. (a) HH polarization and (b) VV polarization.

#### IV. CONCLUSION

In this paper, we have examined the analysis of three-dimensional scattering via the MRTD method, with a Haar-wavelet expansion. Comparisons have been made to data generated via an MoM model [21] and to FDTD-generated data. Several observations can be accrued from these initial studies. First, an advantage of the MRTD is manifested in its natural multigrid capabilities. In particular, within the context of a Haar expansion, regions in which wavelets are employed correspond to cubic sampling at a higher density relative to where scaling functions are used alone. A good example of where such a multiresolution scheme might appear salutary is for subsurface sensing. For such a problem, one can often spatially sample the air region more coarsely than the soil, since the wavelength in air is typically much larger than that in the soil. However, new absorbing-boundary conditions (ABCs), such as the perfectly matched layer [19], [20], are so good that the ABC can be placed

very close to the air–soil interface. Therefore, the air region constitutes a small fraction of the computational domain, realizing less computational benefit to a multiresolution analysis. We found the same to be true of free-space scattering from a dielectric sphere, for example, in which the PML ABC was again placed very close to the target, minimizing the volume occupied in the computational domain by the surrounding air. Nevertheless, there are problems for which such a multiscale analysis is appropriate, e.g., multiple dielectric targets with relatively large intertarget spacing. Moreover, if there is a large contrast between a buried target and the surrounding soil, a multiresolution analysis may again be desirable.

In the examples considered here, in which the targets had a curved surface that did not conform to the Cartesian FDTD or MRTD grid, the principal utility of MRTD was manifested in the handling of general inhomogeneities. As discussed in Section II-B, for regions in the vicinity of discrete dielectric contrasts, the MRTD difference equations are augmented by matrices that account for the material medium. These matrices are easily computed (and stored) within the context of MRTD, and it was demonstrated that in some examples this can lead to significant numerical savings vis-à-vis a traditional (simple) FDTD analysis. In particular, in FDTD one typically samples the computational domain uniformly in space, and therefore the computational complexity is dictated by the smallest scatterer to be discretized. It should be noted that conformal cells have been introduced within the context of FDTD, which could also be employed to handle local curvature [18]. Multigrid FDTD schemes have also been addressed, although these typically require significant care to assure numerical stability [12]–[14]. It is important to emphasize that the examples presented in this paper, comparing FDTD and MRTD, handicapped the FDTD scheme in that the simplest FDTD implementation has been considered. In this context, we note that numerous improvements have been implemented in the FDTD, allowing it to consider multigridding (as mentioned above) as well as conformal meshes [23]–[25].

We have undertaken an initial investigation of the utility of MRTD for three-dimensional scattering problems, employing Haar wavelets. There are many issues that deserve further study. In particular, one of the principal advantages of MRTD involves reduced numerical dispersion compared to FDTD, assuming that higher order wavelets are employed. For example, the Battle–Lemarie wavelets have been demonstrated to yield markedly reduced numerical dispersion relative to FDTD [9], although the integrals required for material inhomogeneity are more complicated than with a Haar expansion. One can also consider a biorthogonal wavelet expansion [10], which offers advantages relative to orthogonal wavelets. Therefore, while a principal utility of MRTD, as investigated here, has centered around the ability to handle general dielectric inhomogeneity, to this advantage can be added reduced numerical dispersion through use of more sophisticated wavelets.

#### REFERENCES

- [1] L. Peters Jr, J. J. Daniels, and J. D. Young, "Ground penetrating radar as an environmental sensing tool," *Proc. IEEE*, vol. 82, pp. 1802–1822, Dec. 1994.
- [2] J. M. Bourgeois and G. S. Smith, "A fully three-dimensional simulation of ground penetrating radar: FDTD theory compared with experiment," *IEEE Trans. Geosci. Remote Sensing*, vol. 34, pp. 36–28, Jan. 1996.
- [3] S. Vitebskiy, K. Sturgess, and L. Carin, "Short-pulse plane-wave scattering from buried perfectly conducting bodies of revolution," *IEEE Trans. Antennas Propagat.*, vol. 44, pp. 143–151, Feb. 1996.
- [4] S. Vitebskiy and L. Carin, "Resonances of perfectly conducting wires and bodies of revolution buried in a lossy dispersive half-space," *IEEE Trans. Antennas Propagat.*, vol. 44, pp. 1575–1583, Dec. 1996.
- [5] T. J. Yu and L. Carin, "Analysis of the electromagnetic inductive response of a void in a conducting-soil background," *IEEE Trans. Geosci. Remote Sensing*, vol. 38, pp. 1320–1327, May 2000.
- [6] N. Geng, A. Sullivan, and L. Carin, "Multilevel fast-multipole algorithm for scattering from conducting targets above or embedded in a lossy half space," *IEEE Trans. Geosci. Remote Sensing*, vol. 38, pp. 1561–1573, July 2000.
- [7] T. P. Montoya and G. S. Smith, "Land mine detection using a ground-penetrating radar based on resistively loaded vee dipoles," *IEEE Trans. Antennas Propagat.*, vol. 47, pp. 1795–1806, Dec. 1999.
- [8] M. Krumpholz and L. Katehi, "MRTD: New time-domain schemes based on multiresolution analysis," *IEEE Trans. Microwave Theory Tech.*, vol. 44, pp. 555–571, 1996.
- [9] E. T. Tentzeris, R. L. Robertson, J. Harvey, and L. Katehi, "Stability and dispersion analysis of Battle-Lemarie based MRTD schemes," *IEEE Trans. Microwave Theory Tech.*, vol. 47, pp. 1004–1013, 1999.
- [10] T. Dogaru and L. Carin, "Multiresolution time-domain using CDF biorthogonal wavelets," *IEEE Trans. Microwave Theory Tech.*, vol. 49, pp. 902–912, May 2001.
- [11] C. S. Burrus, R. A. Gopinath, and H. Guo, *Introduction to Wavelets and Wavelet Transforms: A Primer*. Englewood Cliffs, NJ: Prentice-Hall, 1997.
- [12] M. W. Chevalier, R. J. Luebbers, and V. P. Cable, "FDTD local grid with material traverse," *IEEE Trans. Antennas Propagat.*, vol. 45, pp. 411–421, 1997.
- [13] M. J. White, M. F. Iskander, and Z. Huang, "Development of a multigrid FDTD code for three-dimensional applications," *IEEE Trans. Antennas Propagat.*, vol. 45, pp. 1512–1517, 1997.
- [14] M. Okoniewski, E. Okoniewska, and M. A. Stuchly, "Three-dimensional subgridding algorithm for FDTD," *IEEE Trans. Antennas Propagat.*, vol. 45, pp. 422–429, 1997.
- [15] A. Taflov, *Computational Electrodynamics: The Finite-Difference Time-Domain Method*. Norwood, MA: Artech House, 1995.
- [16] T. Dogaru and L. Carin, "Multiresolution time-domain analysis of scattering from a rough dielectric surface," *Radio Sci.*, vol. 35, pp. 1279–1292, Nov.-Dec. 2000.
- [17] F. D. Hastings, J. B. Schneider, and S. L. Broschat, "A Monte-Carlo FDTD technique for rough surface scattering," *IEEE Trans. Antennas Propagat.*, vol. 43, pp. 1183–1191, 1995.
- [18] T. G. Jurgens, A. Taflov, K. R. Umashankar, and T. G. Moore, "Finite-difference time-domain modeling of curved surfaces," *IEEE Trans. Antennas Propagat.*, vol. 40, pp. 357–366, 1992.
- [19] J. P. Berenger, "A perfectly matched layer for the absorption of electromagnetic waves," *J. Comput. Phys.*, vol. 114, pp. 185–200, 1994.
- [20] J. Fang and Z. Wu, "Generalized perfectly matched layer—An extension of Berenger's perfectly matched layer boundary condition," *IEEE Microwave Guided Wave Lett.*, vol. 5, pp. 451–453, Dec. 1995.
- [21] N. Geng and L. Carin, "Wide-band electromagnetic scattering from a dielectric BOR buried in a layered lossy dispersive medium," *IEEE Trans. Antennas Propagat.*, vol. 47, pp. 610–619, Apr. 1999.
- [22] P. Hubral and M. Tygel, "Analysis of the Rayleigh pulse," *Geophysics*, vol. 54, pp. 654–658, 1989.
- [23] W. H. Yu and R. Mittra, "A conformal FDTD algorithm for modeling perfectly conducting objects with curve-shaped surfaces and edges," *Microwave Opt. Tech. Lett.*, vol. 27, pp. 136–138, Oct. 20, 2000.
- [24] M. W. Yang, Y. C. Chen, and R. Mittra, "Hybrid finite-difference/finite-volume time-domain analysis for microwave integrated circuits with curved PEC surfaces using a nonuniform rectangular grid," *IEEE Trans. Microwave Theory Tech.*, vol. 48, pp. 969–975, June 2000.
- [25] M. Celuch-Marcysiak and W. K. Gwarek, "Improved and simpler FDTD formulation for axisymmetrical problems," in *IEEE Antennas Propagation Soc. Int. Symp.*, vol. 1, 2000, pp. 31–31.



**Xianyang Zhu** (M'01) was born in Anhui, China, in 1967. He received the B.S. and Ph.D. degrees in electrical engineering from Xi'an Jiaotong University, Xi'an, China, in 1988 and 1994, respectively.

Since March 1999, he has been a Research Associate in the Center for Applied Remote Sensing, Department of Electrical and Computer Engineering, Duke University, Durham, NC. From November 1997 to February 1999, he was a Postdoctoral Research Fellow with the Center for Computational Electromagnetics, Department of Electrical and

Computer Engineering, University of Illinois at Urbana-Champaign. From 1994 to 1997, he was with the Electromagnetics Institute, Southwest Jiaotong University, where he became an Associate Professor in 1995. His main research interests include computational electromagnetics, radar cross-section analysis, electromagnetic compatibility, and antennas analysis.

**Lawrence Carin** (SM'96-F'01) was born on March 25, 1963, in Washington, DC. He received the B.S., M.S., and Ph.D. degrees in electrical engineering from the University of Maryland, College Park, in 1985, 1986, and 1989, respectively.

In 1989, he joined the Electrical Engineering Department, Polytechnic University, Brooklyn, NY, as an Assistant Professor. He became an Associate Professor there in 1994. In September 1995, he joined the Electrical Engineering Department, Duke University, Durham, NC, where he is now a Professor. He is the Principal Investigator on a Multidisciplinary University Research Initiative (MURI) on demining. His current research interests include short-pulse scattering, subsurface sensing, and wave-based signal processing.

Prof. Carin is a member of Tau Beta Pi and Eta Kappa Nu. He is an Associate Editor of the IEEE TRANSACTIONS ON ANTENNAS AND PROPAGATION.